

## PAPER

[View Article Online](#)  
[View Journal](#) | [View Issue](#)Cite this: *Ind. Chem. Mater.*, 2024, 2, 432

## Triphase photocatalytic water-gas-shift reaction for hydrogen production with enhanced interfacial diffusion at gas–liquid–solid interfaces†

Huige Chen,<sup>ab</sup> Zhenhua Li,<sup>a</sup> Chao Zhou, <sup>a</sup> Run Shi <sup>\*a</sup> and Tierui Zhang <sup>\*ab</sup>

The exothermic characteristic of the water-gas-shift (WGS) reaction, coupled with the thermodynamic constraints at elevated temperatures, has spurred a research inclination towards conducting the WGS reaction at reduced temperatures. Nonetheless, the challenge of achieving efficient mass transfer between gaseous CO and liquid H<sub>2</sub>O at the photocatalytic interface under mild reaction conditions hinders the advancement of the photocatalytic WGS reaction. In this study, we introduce a gas–liquid–solid triphase photocatalytic WGS reaction system. This system facilitates swift transportation of gaseous CO to the photocatalyst's surface while ensuring a consistent water supply. Among various metal-loaded TiO<sub>2</sub> photocatalysts, Rh/TiO<sub>2</sub> nanoparticles positioned at the triphase interface demonstrated an impressive H<sub>2</sub> production rate of 27.60 mmol g<sup>−1</sup> h<sup>−1</sup>. This rate is roughly 2 and 10 times greater than that observed in the liquid–solid and gas–solid diphasic systems. Additionally, finite element simulations indicate that the concentrations of CO and H<sub>2</sub>O at the gas–liquid–solid interface remain stable. This suggests that the triphase interface establishes a conducive microenvironment with sufficient CO and H<sub>2</sub>O supply to the surface of photocatalysts. These insights offer a foundational approach to enhance the interfacial mass transfer of gaseous CO and liquid H<sub>2</sub>O, thereby optimizing the photocatalytic WGS reaction's efficiency.

Keywords: Water-gas-shift; Photocatalysis; Triphase interface; Hydrogen evolution; TiO<sub>2</sub>.Received 28th December 2023,  
Accepted 19th February 2024

DOI: 10.1039/d3im00135k

rsc.li/icm

## 1 Introduction

Hydrogen (H<sub>2</sub>) stands as a pivotal renewable chemical with extensive applications in contemporary society.<sup>1–3</sup> Currently, the predominant method for H<sub>2</sub> production involves the steam reforming of hydrocarbons derived from fossil fuels.<sup>4,5</sup> Nevertheless, this steam reforming technique demands elevated temperatures and pressures, leading to substantial costs and energy expenditures. Furthermore, the H<sub>2</sub> generated often retains elevated levels of CO, rendering it less suitable for subsequent industrial applications.<sup>5</sup>

The water-gas-shift (WGS) reaction (CO + H<sub>2</sub>O → CO<sub>2</sub> + H<sub>2</sub>) holds significant importance in the chemical industry, serving multiple functions such as H<sub>2</sub> production, CO removal, and syngas adjustment.<sup>6–8</sup> Over recent decades, considerable research has centered on the thermocatalytic

WGS reaction.<sup>9–12</sup> Typically, thermocatalytic WGS transpires at temperatures ranging from 180–230 °C for noble metal catalysts, while non-precious metal catalysts necessitate even higher temperatures, surpassing 270 °C.<sup>9,13–16</sup> Nonetheless, the reaction's exothermic nature coupled with thermodynamic constraints at elevated temperatures has spurred increased exploration into the WGS reaction at lower temperatures.

Photocatalysis has garnered extensive attention across various chemical reactions, presenting numerous advantages over conventional thermocatalysis. A primary advantage of photocatalysis lies in its mild reaction conditions and reduced reliance on fossil fuels, as it directly utilizes solar energy to drive reactions.<sup>17,18</sup> Utilizing metal oxide semiconductors like TiO<sub>2</sub>, CuO<sub>x</sub>, among others, in photocatalysis offers a compelling approach to lowering the WGS reaction temperature to ambient levels.<sup>19,20</sup>

Presently, the photocatalytic WGS reaction predominantly operates within a gas–solid (G–S) diphasic system, employing gaseous CO and water vapor as reactants.<sup>19,21</sup> However, at lower temperatures, the constrained saturated vapor pressure of water can impede its interfacial mass transfer, potentially becoming the rate-determining step. Furthermore, water molecules interconnected *via* hydrogen bonds exhibit

<sup>a</sup> Key Laboratory of Photochemical Conversion and Optoelectronic Materials, Technical Institute of Physics and Chemistry, Chinese Academy of Sciences, Beijing 100190, China. E-mail: shirun@mail.ipc.ac.cn, tierui@mail.ipc.ac.cn

<sup>b</sup> Center of Materials Science and Optoelectronics Engineering, University of Chinese Academy of Sciences, Beijing 100049, China

† Electronic supplementary information (ESI) available. See DOI: <https://doi.org/10.1039/d3im00135k>



superior water-splitting capabilities compared to their isolated counterparts.<sup>22</sup> This suggests that liquid water might serve as a more effective reactant source than water vapor for low-temperature WGS reaction. Notably, under standard conditions (25 °C, 1 atm), CO molecules demonstrate limited solubility ( $\sim 1$  mM) and a modest diffusion coefficient ( $2.03 \times 10^{-5} \text{ cm}^2 \text{ s}^{-1}$ ) in the aqueous phase.<sup>23,24</sup> This implies that in liquid-solid (L-S) diphasic photocatalytic systems, which has been widely investigated for decades, the WGS reaction might be hindered by the interfacial mass transfer of CO molecules. Effectively enhancing both the mass transfer and the chemical reaction between gaseous CO and liquid H<sub>2</sub>O at the photocatalytic interface presents a complex challenge.

Recently, the scientific community has delved into photocatalysis at gas-liquid-solid (G-L-S) triphase interfaces. This approach has demonstrated distinct advantages in various photocatalytic reactions involving both gas and water reactants, such as CO<sub>2</sub> reduction, active oxygen generation, and ethylene purification.<sup>25–27</sup> By facilitating the diffusion of CO and H<sub>2</sub>O to the photocatalyst surface *via* both gaseous and liquid phases, the WGS reaction at G-L-S interfaces holds promise in overcoming the constraints observed in diphasic systems, potentially enhancing the overall H<sub>2</sub> production efficiency under mild reaction conditions.

In this study, we introduce a triphase photocatalytic system tailored for the WGS reaction, leveraging metal-loaded TiO<sub>2</sub> (M/TiO<sub>2</sub>, where M represents Rh, Au, Ag, Pt, and Pd) as the benchmark photocatalysts. To realize this setup, a hydrophobic porous layer served as the support, enabling the

photocatalysts to float at the gas-water interface and fostering abundant G-L-S interfaces. Among tested photocatalysts, Rh/TiO<sub>2</sub> demonstrated the highest H<sub>2</sub> production rate of  $27.60 \text{ mmol g}^{-1} \text{ h}^{-1}$ . Remarkably, this rate surpasses that of both the corresponding L-S and G-S diphasic systems by factors of approximately 2 and 10, respectively. Finite element simulations reveal consistent concentrations of CO and H<sub>2</sub>O at the G-L-S interface during the photocatalytic diffusion-reaction process, although a significant decline in CO is evident at the L-S interface. This observation aligns with the elevated H<sub>2</sub> production rates observed in the triphase system when utilizing diluted CO (0.02 MPa) as the gaseous feedstock. Serving as a proof-of-concept, our results underscore the pivotal role of the G-L-S triphase interface in augmenting the interfacial mass transfer and reaction of gaseous CO and liquid H<sub>2</sub>O, thereby enhancing the efficiency of the photocatalytic WGS reaction.

## 2 Results and discussion

The structural characteristics and surface morphology of the Rh/TiO<sub>2</sub> photocatalysts were systematically examined, as depicted in Fig. 1. The X-ray diffraction (XRD) profile of *x* wt% Rh/TiO<sub>2</sub> (*x* = 1, 3, 5, 7, and 9) reveals the presence of both anatase TiO<sub>2</sub> (JCPDS no. 73-1764) and rutile TiO<sub>2</sub> (JCPDS no. 87-0710). Notably, no discernible signal corresponding to metallic Rh was observed across all Rh/TiO<sub>2</sub> samples (Fig. 1a). This absence could be attributed to the small crystal dimensions and the relatively modest Rh content.<sup>28</sup> The

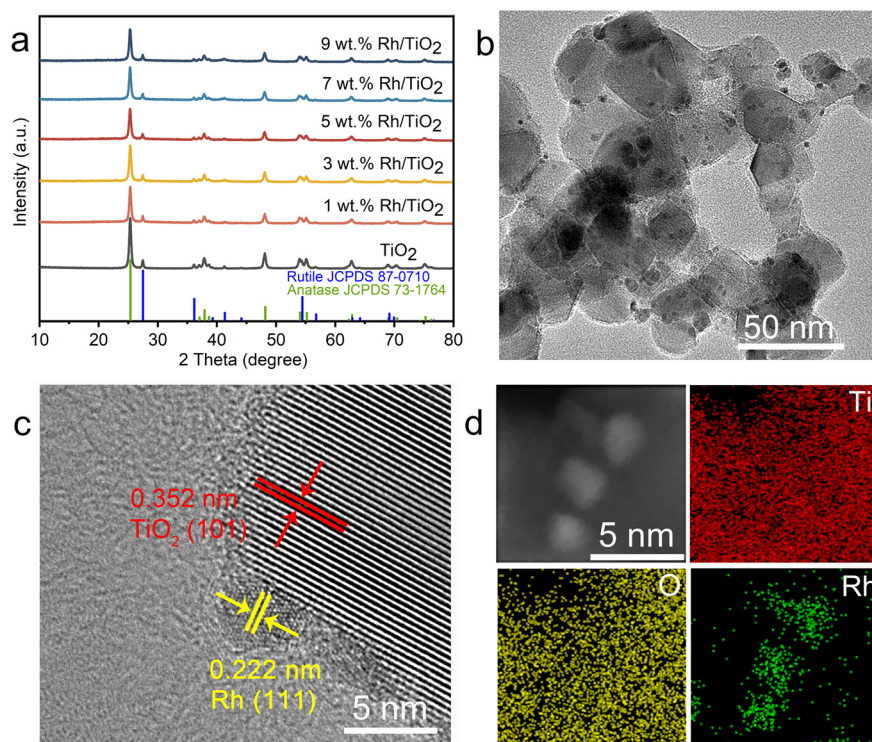


**Fig. 1** Characterization for Rh/TiO<sub>2</sub> photocatalysts. (a) XRD pattern for *x* wt% Rh/TiO<sub>2</sub>; (b) TEM image and (c) high-resolution TEM image of 5 wt% Rh/TiO<sub>2</sub>; (d) the HAADF-STEM image and EDS element maps of 5 wt% Rh/TiO<sub>2</sub>.



experimental loading content of Rh within  $\text{TiO}_2$  align closely with the theoretical values (Fig. S1†). 5 wt% Rh/ $\text{TiO}_2$  was utilized throughout unless otherwise stated. Upon examination *via* transmission electron microscopy (TEM) and high-resolution TEM, Rh nanoparticles, each having a diameter of approximately  $2.0 \pm 0.5$  nm, were found to be uniformly dispersed over the  $\text{TiO}_2$  surface (Fig. 1b and S2†). The observed lattice spacings of 0.352 nm and 0.222 nm correspond to the *d*-spacing values of  $\text{TiO}_2$  (101) and Rh (111), respectively (Fig. 1c). Moreover, high-angle annular dark-field scanning TEM (HAADF-STEM) coupled with energy-dispersive X-ray spectroscopy (EDS) elemental mapping corroborates the distinct spatial distribution of Rh nanoparticles on  $\text{TiO}_2$  (Fig. 1d).

Polytetrafluoroethylene gas diffusion layers (GDL) served as the porous substrates for the immobilization of the photocatalyst. Rh/ $\text{TiO}_2$  was anchored onto the GDL using a vacuum filtration method, denoted as Rh/ $\text{TiO}_2$ -GDL. The structure of Rh/ $\text{TiO}_2$ -GDL is evident in the cross-sectional scanning electron microscopy (SEM) image presented in Fig. 2a. The corresponding EDS mapping, highlighting Ti, C, and F elements, provides insights into the photocatalyst layer's thickness, which is approximately  $1.4 \pm 0.2$   $\mu\text{m}$  (Fig. 2b). The top-view SEM reveals a distinct cross-linked fibre network within the porous substrate, establishing abundant pores for efficient gas diffusion (Fig. 2c). The inset of Fig. 2c displays a water droplet contact angle of  $126^\circ$ , underscoring the inherent hydrophobic nature of the GDL porous substrate. After the immobilization of Rh/ $\text{TiO}_2$ , the resultant photocatalyst layer exhibits a significantly reduced water contact angle of  $19^\circ$ , indicating a pronounced hydrophilic-hydrophobic transition within the Rh/ $\text{TiO}_2$ -GDL layered structure (Fig. 2d).

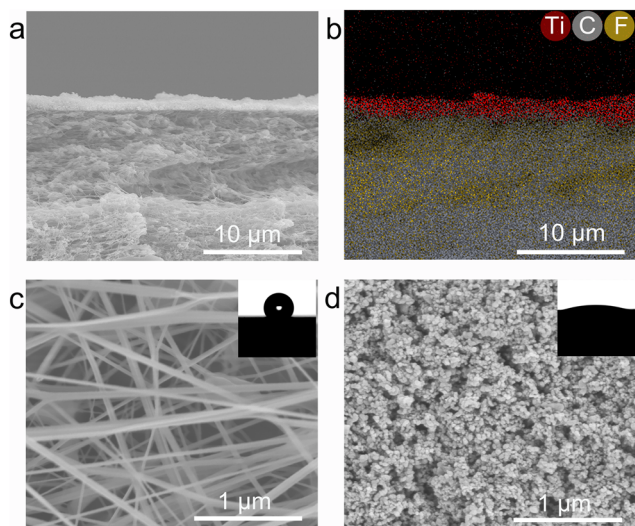


**Fig. 2** Structural characterization of the Rh/ $\text{TiO}_2$ -GDL. (a) Cross-sectional SEM image and (b) corresponding EDS mapping of Rh/ $\text{TiO}_2$ -GDL; top-view SEM images of (c) pristine GDL porous substrate and (d) immobilized Rh/ $\text{TiO}_2$  photocatalyst layer. Inserts in (c) and (d) show photographs of water droplets on each sample.

As illustrated in Fig. 3a, both pristine  $\text{TiO}_2$  and all *x* wt% Rh/ $\text{TiO}_2$  samples exhibit pronounced absorption in the ultraviolet region, attributed to the characteristic edge adsorption of  $\text{TiO}_2$ . The visible light absorption, corresponding to Rh nanoparticles, amplifies with increasing Rh loading. To further discern the influence of different metal species on the WGS reaction, other M/ $\text{TiO}_2$  (where M = Au, Ag, Pt, and Pd) with a consistent metal loading of 5 wt% were synthesized using analogous procedures. The XRD patterns exhibit characteristic peaks corresponding to anatase  $\text{TiO}_2$  (JCPDS no. 73-1764) and rutile  $\text{TiO}_2$  (JCPDS no. 87-0710), while characteristic peaks corresponding to metal are notably absent, possibly attributable to the small crystal dimensions (Fig. S3†). The TEM images confirm the successful loading of metal nanoparticles onto  $\text{TiO}_2$  for all M/ $\text{TiO}_2$  samples (Fig. S4†). The achieved metal content closely aligns with theoretical predictions (Fig. S5†), with all samples demonstrating robust optical absorption below 400 nm (Fig. S6†). Consequently, a 365 nm LED lamp was employed as the illumination source to assess the photocatalytic efficiency. The  $\text{H}_2$  production rates of Rh/ $\text{TiO}_2$  and the other M/ $\text{TiO}_2$  photocatalysts in the G-L-S triphase system are depicted in Fig. 3b.  $\text{TiO}_2$  modified with distinct metals showcases marked variations in  $\text{H}_2$  production rates under both CO (WGS) and Ar (pure water splitting) gas phase conditions. In an Ar environment, Pt/ $\text{TiO}_2$  achieves the highest  $\text{H}_2$  production rate of  $5.95 \text{ mmol g}^{-1} \text{ h}^{-1}$ , consistent with prior studies employing Pt as co-catalysts for photocatalytic water splitting.<sup>29–31</sup> However, transitioning to a CO environment only results in a slight enhancement over Pt/ $\text{TiO}_2$ , suggesting a minimal contribution of the WGS reaction to  $\text{H}_2$  generation. Conversely, Rh/ $\text{TiO}_2$  registers a five-fold enhancement in  $\text{H}_2$  production rate ( $25.77 \text{ mmol g}^{-1} \text{ h}^{-1}$ ) compared to its performance in an Ar condition, underscoring the pivotal role of CO in enhancing generating  $\text{H}_2$  *via* the WGS pathway. A pronounced boost was also observed for Au/ $\text{TiO}_2$  ( $13.77 \text{ mmol g}^{-1} \text{ h}^{-1}$ ), with the  $\text{H}_2$  production trend across M/ $\text{TiO}_2$  as follows: Rh/ $\text{TiO}_2$  > Au/ $\text{TiO}_2$  > Pt/ $\text{TiO}_2$  > Ag/ $\text{TiO}_2$  > Pd/ $\text{TiO}_2$ . The observed disparities in  $\text{H}_2$  production rates among various M/ $\text{TiO}_2$  samples in different gas conditions likely stem from the synergistic interplay between CO adsorption and proton reduction kinetics at the metal active sites.<sup>32,33</sup>

The loading amount of Rh within Rh/ $\text{TiO}_2$  significantly impacts its photocatalytic WGS efficiency. As depicted in Fig. 3c, the  $\text{H}_2$  production rate escalates progressively from 15.10 to  $28.17 \text{ mmol g}^{-1} \text{ h}^{-1}$  with Rh loadings escalating from 1 wt% to 5 wt%. However, augmenting the Rh content beyond 5 wt% only marginally enhances the  $\text{H}_2$  production rate. Consequently, 5 wt% Rh-loaded Rh/ $\text{TiO}_2$  was adopted for subsequent experiments. Subsequently, a photostability assessment was conducted on Rh/ $\text{TiO}_2$  within the G-L-S photocatalytic system. Under continuous irradiation for 5 hours, the  $\text{H}_2$  production rate shows a linear correlation with irradiation time, culminating in a cumulative yield of  $111.52 \text{ mmol g}^{-1}$  (Fig. S7†). Additionally, Fig. 3d underscores that





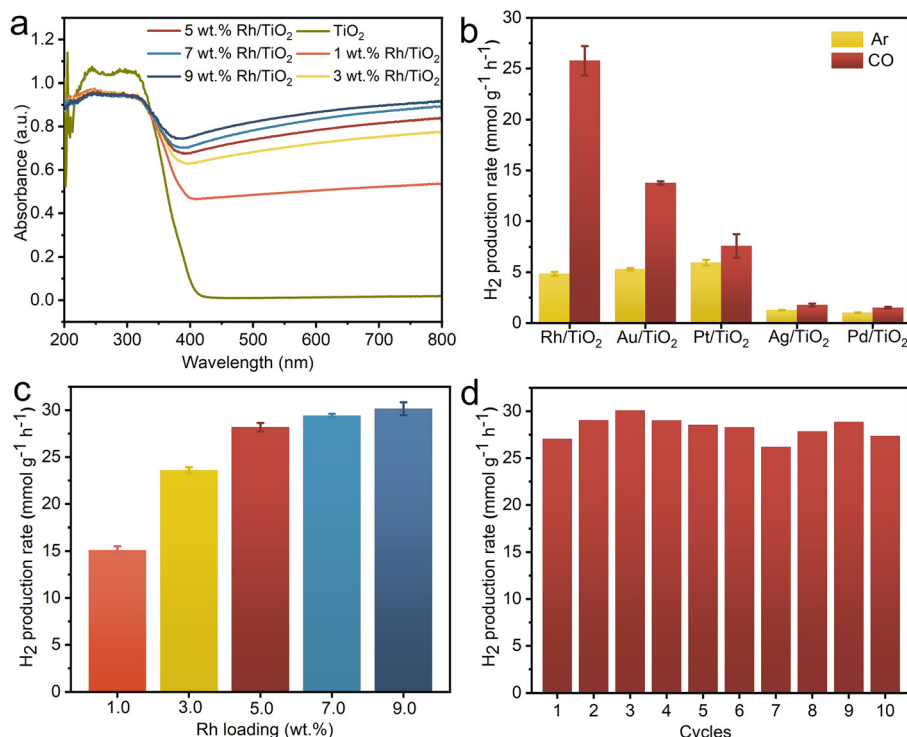


**Fig. 3** (a) Absorption spectra for TiO<sub>2</sub> and *x* wt.% Rh/TiO<sub>2</sub>; (b) triphase photocatalytic H<sub>2</sub> production rate for 5 wt.% M/TiO<sub>2</sub> (M = Rh, Au, Ag, Pt, Pd) in Ar or CO atmosphere; (c) photocatalytic H<sub>2</sub> production rate as a function of the loading amount of Rh in Rh/TiO<sub>2</sub>; (d) cycling tests for Rh/TiO<sub>2</sub>. Reaction conditions: gas phase = 0.2 MPa of CO, liquid phase = 10 mL of H<sub>2</sub>O, solid phase = 2 mg of photocatalyst immobilized on GDL (4 cm in diameter), light source = 365 nm LED (300 mW cm<sup>-2</sup>). Error bars represent the standard deviation from at least three independent measurements.

the H<sub>2</sub> production activity of the Rh/TiO<sub>2</sub> photocatalyst remains consistent after 10 photocatalytic cycles (1 h for each

cycle, 10 h in total). Notably, the structure and morphology of the Rh/TiO<sub>2</sub> photocatalyst show no obvious change after the

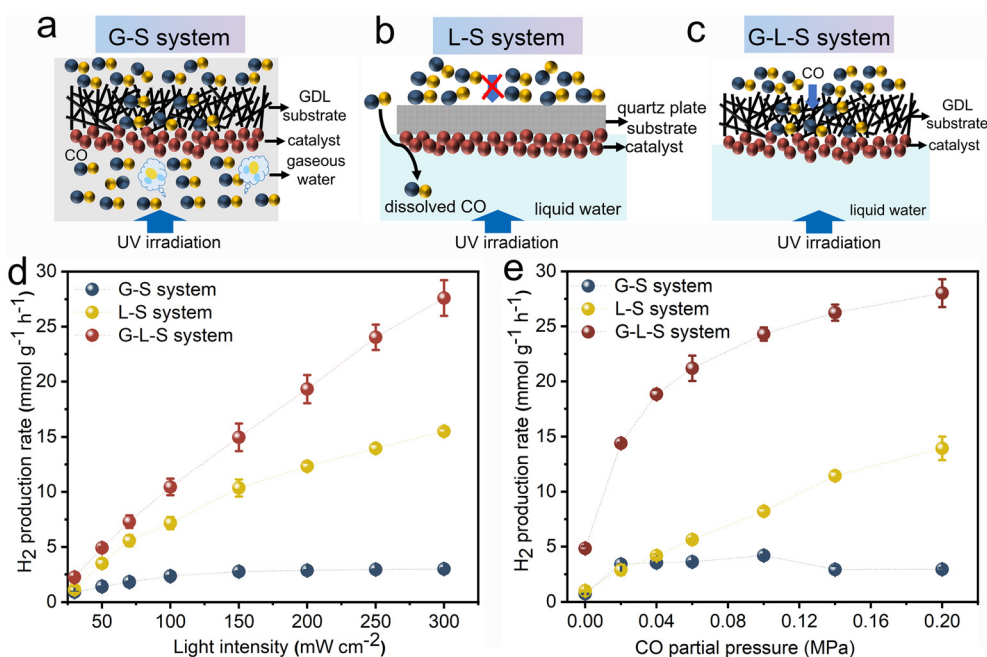


**Fig. 4** Schematic illustration of (a) G-S, (b) L-S, and (c) G-L-S systems; (d) light intensity-dependent photocatalytic H<sub>2</sub> production rate over Rh/TiO<sub>2</sub> at a CO partial pressure of 0.2 MPa; (e) CO partial pressure-dependent photocatalytic H<sub>2</sub> production rate at a light intensity of 300 mW cm<sup>-2</sup>. Error bars represent the standard deviation from at least three independent measurements.



cycling test (Fig. S8 and S9†), signify its commendable photostability. The contact angle of water droplets on the GDL porous substrate did not show a significant change after the cycling experiment (Fig. S10†), indicating its stable hydrophobicity.

The photocatalytic WGS reaction was examined across various triphase and diphasic systems using Rh/TiO<sub>2</sub> as the photocatalyst. Schematic illustrations of the G-S and L-S diphasic system and the G-L-S triphase system are provided in Fig. 4a-c. For the G-S system (Fig. 4a), which is a configuration frequently employed in conventional (photo) thermal WGS reactions, the CO reactant can directly diffuse to the photocatalyst from the gas phase. The water concentration within this gas phase is standardized at 0.95 mM, representing 74% of the relative humidity at room temperature. Fig. 4b showcases the L-S system where Rh/TiO<sub>2</sub> is immobilized onto a quartz plate instead of the GDL porous substrate. Here, CO from the gas phase dissolves and undergoes a long-range diffusion process within the aqueous phase to reach the photocatalyst. In the G-L-S system, as depicted in Fig. 4c, gaseous CO traverses to the photocatalyst's surface *via* the hydrophobic GDL pores. Simultaneously, a high interfacial water concentration (equivalent to 55.6 M for pure water) is maintained at ambient conditions. This ensures an optimized diffusion-reaction process for both CO and H<sub>2</sub>O molecules during the photocatalytic WGS reaction.

The photocatalytic WGS reaction activities across the three systems were investigated using light intensity and CO partial pressure as variables. As depicted in Fig. 4d, the light intensity-dependent behaviour of the photocatalytic WGS reaction was evaluated at a constant CO partial pressure of 0.2 MPa. Within the G-S system, the WGS reaction performance remained largely insubstantial across the tested light intensities (30–300 mW cm<sup>-2</sup>). This minimal activity could be attributed to certain limiting factors. In the L-S system, the H<sub>2</sub> production rate surged to 7.16 mmol g<sup>-1</sup> h<sup>-1</sup> at an intensity of 100 mW cm<sup>-2</sup>, but only experienced a twofold increase upon elevating the intensity to 300 mW cm<sup>-2</sup>. These findings imply that at higher light intensities, the rate-determining step potentially shifts to the mass transfer of CO, given the rapid depletion of reactants. Conversely, within the G-L-S system, the H<sub>2</sub> production rate exhibited a nearly linear augmentation even under elevated light intensities. This behaviour suggests that the rate-limiting steps are more associated with the photo-generation and subsequent separation of charge carriers, rather than the mass transfer process. Notably, the H<sub>2</sub> production rate within the triphase system reached 27.60 mmol g<sup>-1</sup> h<sup>-1</sup> at 300 mW cm<sup>-2</sup>, marking an approximately twofold and tenfold enhancement compared to the L-S and G-S diphasic systems, respectively.

Subsequently, the impact of CO partial pressure on the photocatalytic WGS reaction was assessed with a consistent light intensity set at 300 mW cm<sup>-2</sup>, as illustrated in Fig. 4e. In the G-S system, escalating CO partial pressures did not

yield any discernible increase in activity, aligning with prior observations. In contrast, the L-S system showcased a nearly proportional correlation between the H<sub>2</sub> production rate and CO partial pressure, peaking at 13.93 mmol g<sup>-1</sup> h<sup>-1</sup> at 0.2 MPa. These findings indicate an increased solubility of CO molecules in the aqueous phase and an enhanced mass transfer, both of which correlate positively with elevated CO partial pressures in the connected gas phase. Within the G-L-S system, the H<sub>2</sub> production rate witnessed a marked surge at modest CO partial pressures, outperforming the L-S system at a 10 times reduced CO partial pressure of 0.02 MPa (14.37 mmol g<sup>-1</sup> h<sup>-1</sup>). This underscores the G-L-S system's advantage in selectively converting low-concentration CO, positioning potential applications like CO removal in fuel cells (for hydrogen purification) and mitigating CO poisoning risks in confined environments. However, the rate of enhancement decelerates at elevated CO partial pressures, indicative of a transition in the rate-determining step, potentially shifting from CO mass transfer to other processes, such as the photo-generation and subsequent separation of charge carriers.

A three-dimensional finite element method (FEM) simulation was employed to computationally elucidate the interfacial mass transfer of CO and H<sub>2</sub>O across various reaction systems. As depicted in the left panel of Fig. 5, three distinct models were constructed to represent the G-S (top), L-S (middle), and G-L-S (bottom) systems. In the G-L system, the simulation focused on the local H<sub>2</sub>O concentration, with an initial concentration set at 0.95 mM based on experimental data. For both the L-S and G-L-S systems, the simulation targeted the local CO concentration, with the initial concentration determined by the saturated solubility of CO within the aqueous phase (1.01 mM).<sup>23</sup> The FEM simulation aimed to capture the diffusion-reaction dynamic process occurring at the reaction interface. To align with the optimized photocatalytic H<sub>2</sub> production rates observed in the G-L-S system (approximately 10 mM s<sup>-1</sup>), the consumption rates of CO and H<sub>2</sub>O within the photocatalytic layer region were modulated, ranging from 5 to 15 mM s<sup>-1</sup>.

The *xz* diagrams depicting the simulated reactant concentrations for the G-S, L-S, and G-L-S systems are illustrated in Fig. 5a-c, respectively. In the G-S system (Fig. 5a), the local water vapor concentration within the photocatalyst layer exhibits minimal decline even at escalated H<sub>2</sub>O consumption rates. This observation implies that the subdued H<sub>2</sub> production in the G-S setup might not be directly attributable to interfacial diffusion or mass transfer challenges of water molecules. Instead, it could be linked to the adverse impact of water vapor, characterized by a weak hydrogen bond network, on H<sub>2</sub> production, as previously suggested.<sup>22</sup> In the L-S system (Fig. 5b), where the photocatalyst layer is submerged within a bulk water phase, the local CO concentration surrounding the catalyst surface diminishes markedly with the rising CO consumption rate. However, the G-L-S configuration (Fig. 5c) showcases a consistent CO concentration even at elevated consumption





**Fig. 5** Schematic diagrams and FEM simulation results of (a) G–S, (b) L–S, and (c) G–L–S systems. The colour scale in (a) represents the water vapor concentration, in (b) and (c) represents the CO concentration.

rates. This stability underscores the function of the triphase interface in maintaining a robust supply of CO molecules within the local reaction microenvironment. Such consistent CO availability ensures efficient  $\text{H}_2$  production *via* the photocatalytic WGS pathway, even when subjected to diluted CO conditions.

### 3 Conclusions

In summary, we have developed a G–L–S triphase photocatalytic system utilizing  $\text{M}/\text{TiO}_2$  (where  $\text{M} = \text{Rh}, \text{Au}, \text{Ag}, \text{Pt}, \text{and Pd}$ ) immobilized on a hydrophobic porous GDL for the WGS reaction under ambient conditions. Among the tested catalysts,  $\text{Rh}/\text{TiO}_2$  exhibited the most impressive photocatalytic  $\text{H}_2$  production rate, registering at  $27.60 \text{ mmol g}^{-1} \text{ h}^{-1}$ . This catalyst not only showcased commendable photostability but also displayed remarkable enhancements, even when utilizing gas sources with low CO concentrations. Crucially, the G–L–S configuration notably enhances the mass transfer of both CO and  $\text{H}_2\text{O}$  to the photocatalyst surface, which appears to be the primary rate-determining step. Consequently, this design exhibited  $\text{H}_2$  production rates that were 10 and 2 times higher than those observed in conventional G–S and L–S diphasic systems, respectively. FEM simulations provided insights into the interfacial mass transfer process of CO and  $\text{H}_2\text{O}$ . These findings underscore the triphase system's distinct advantage in ensuring a consistent CO supply to the photocatalyst layer, especially under low-concentration conditions. Overall, our

research underscores the promising potential of the G–L–S triphase photocatalytic system, highlighting its capability to optimize the diffusion–reaction interplay in the WGS process, thereby achieving superior  $\text{H}_2$  production efficiencies under mild conditions.

## 4 Experimental section

### 4.1 Chemicals and materials

$\text{TiO}_2$  (P25) was purchased from Degussa AG.  $\text{RhCl}_3 \cdot 3\text{H}_2\text{O}$  was obtained from Bide Pharmatech Ltd. (China).  $\text{HAuCl}_4 \cdot 4\text{H}_2\text{O}$ ,  $\text{H}_2\text{PtCl}_6 \cdot 6\text{H}_2\text{O}$ , and  $\text{Na}_2\text{PdCl}_4$  were purchased from Aladdin (Shanghai, China).  $\text{AgNO}_3$  was purchased from Sinopharm Chemical Reagent Corporation (Shanghai, China).  $\text{NaBH}_4$  was purchased from Guangdong Guanghua Chemical Factory Co., Ltd. Polytetrafluoroethylene GDL with a thickness of  $30 \mu\text{m}$  and a diameter of  $47 \text{ mm}$  (Chuangwei Filter Media, China) was used as a porous support for photocatalyst immobilization. All chemicals were analytically pure and had not been further purified. Deionized water was used in the whole experiments.

### 4.2 Photocatalyst preparation

**Preparation of  $\text{M}/\text{TiO}_2$ :**  $\text{M}/\text{TiO}_2$  with varying weight loadings were synthesized using the  $\text{NaBH}_4$  reduction method as described by Zhang.<sup>34</sup> Specifically, for the preparation of  $\text{Rh}/\text{TiO}_2$ ,  $200 \text{ mg}$  of  $\text{TiO}_2$  was dispersed in  $100 \text{ mL}$  of water using ultrasonication for  $30 \text{ minutes}$ . Subsequently, different volumes of an aqueous  $\text{RhCl}_3 \cdot 3\text{H}_2\text{O}$  solution (with a



concentration of 10 mg mL<sup>-1</sup> for Rh) were introduced to the aforementioned dispersion and sonicated for another 30 minutes. Following this, a surplus NaBH<sub>4</sub> solution (concentration: 2.5 mg mL<sup>-1</sup>) was meticulously added dropwise to the suspension with continuous stirring. After an additional hour of stirring, the samples underwent centrifugation, followed by rinsing with neutral water. They were then subjected to overnight vacuum freeze-drying. The resulting catalysts were denoted as *x* wt% Rh/TiO<sub>2</sub> (*x* = 1, 3, 5, 7, and 9, representing the theoretical weight ratio of Rh loadings). A consistent synthesis approach was adopted for other M/TiO<sub>2</sub> variants, employing appropriate aqueous solutions of HAuCl<sub>4</sub>·4H<sub>2</sub>O, AgNO<sub>3</sub>, H<sub>2</sub>PtCl<sub>6</sub>·6H<sub>2</sub>O, and Na<sub>2</sub>-PdCl<sub>4</sub> for the synthesis of Au/TiO<sub>2</sub>, Ag/TiO<sub>2</sub>, Pt/TiO<sub>2</sub>, and Pd/TiO<sub>2</sub>, respectively.

Preparation of M/TiO<sub>2</sub>-GDL: taking Rh/TiO<sub>2</sub> as an example, the ethanol dispersion of Rh/TiO<sub>2</sub> (concentration: 0.1 mg mL<sup>-1</sup>) was subjected to sonication for approximately 30 minutes. Subsequently, 20 mL of this suspension was applied to the GDL surface *via* vacuum filtration, resulting in a circular photocatalyst layer with a diameter of 4 cm. After a 1 hour drying period in an oven, Rh/TiO<sub>2</sub>-GDL with a loading density of 0.16 mg cm<sup>-2</sup> was obtained (Fig. S11a†). This layer was then utilized for both the G-L-S and G-S systems. For the L-S system, a 20 mL ethanol dispersion of Rh/TiO<sub>2</sub> (concentration: 0.1 mg mL<sup>-1</sup>) was dripped onto the surface of a circular quartz substrate (4 cm in diameter), followed by a 1 hour drying process in an oven (Fig. S11b†).

### 4.3 Characterization

The structure and crystallization of the particles were provided by XRD (Bruker AXSD8 Advance, Germany). Sample morphologies were examined using SEM (S4800, Hitachi, Japan) and TEM (JEOL-2100F, Japan), both of which were equipped with EDS for elemental analysis. The diffuse reflection spectra of the photocatalyst powders were measured using an ultraviolet-visible spectrophotometer (Cary 7000, Agilent, USA) with an integrating sphere attachment. A contact angle system (OCA20, Dataphysics, Germany) was used to measure the contact angles, with the probe liquid being a 2.0 µL droplet of water.

### 4.4 Photocatalytic measurements

Photocatalytic WGS reaction measurements: The photocatalytic activities of the synthesized samples were evaluated using a custom-built photocatalytic reactor (Fig. S12 and S13†). A 365 nm LED (PLS-LED100C, PerfectLight, China), paired with a  $\lambda < 400$  nm filter (Xujiang Electromechanical Plant, Nanjing, China), served as the illumination source. In the G-S configuration, the Rh/TiO<sub>2</sub>-GDL was positioned within the reactor. CO (99.99%) was then bubbled through a water tank, producing a CO/water gas mixture under atmospheric conditions. The humidified CO was introduced into the reactor at a flow rate of 400 mL min<sup>-1</sup> for 30 minutes, achieving a water vapor concentration

of 0.95 mM (equivalent to 74% relative humidity). Subsequently, the reaction gas was introduced to elevate the pressure to 0.2 MPa. For the L-S system, the Rh/TiO<sub>2</sub>-immobilized quartz plate was submerged in 10 mL of water. For the G-L-S system, the Rh/TiO<sub>2</sub>-GDL was positioned above a 10 mL water surface. Both L-S and G-L-S systems were pressurized to 0.20 MPa with CO gas and then sealed. After a 1 hour irradiation period, the WGS reaction products were quantified using a gas chromatograph (GC-2014C, Shimadzu, Japan) equipped with a TCD detector, molecular sieve 5, and utilizing N<sub>2</sub> as the carrier gas. For the photocatalytic cycling stability experiment, reaction products were quantitatively analysed using a gas chromatograph after 1 hour of irradiation. Subsequently, the gas within the photocatalytic reactor was entirely exhausted and replaced with CO for the subsequent cycle. This cycle was repeated ten times.

Light intensity and CO partial pressure modulation: Experiments were conducted to assess the light intensity dependence in the photocatalytic WGS reaction, maintaining a constant CO partial pressure of 0.2 MPa. The varying light intensities were achieved by modulating the output power of the 365 nm LED. Additionally, tests at different CO partial pressures were performed under a steady light intensity of 300 mW cm<sup>-2</sup>. The CO partial pressures were adjusted by manipulating the CO/Ar volume ratio at a consistent total pressure of 0.2 MPa.

### 4.5 FEM simulation

The mass transfer and consumption behaviours of CO and H<sub>2</sub>O in the G-S, L-S, and G-L-S systems were analysed *via* Fick's second law using FEM simulations conducted in COMSOL 5.4. Fick's second law is as follows:

$$\frac{\partial C_i}{\partial t} + \nabla \cdot \mathbf{J}_i + u \cdot \nabla C_i = R_i \quad (1)$$

$$\mathbf{J}_i = -D_i \nabla C_i, u = \frac{x}{\sqrt{t}} \quad (2)$$

$C_i$  is the concentration of dimensions,  $t$  is the time,  $D_i$  is the diffusion coefficient in dimensions,  $\nabla C_i$  is the Laplacian, and  $x$  is the distance. The three-dimensional geometric models of these systems were 500 µm × 500 µm × 400 µm (Fig. S14†). In the G-S system, the sequence from top to bottom comprises the gas phase, the photocatalyst layer, and the gas phase. The water vapor concentrations on both the upper and lower surfaces were set to 0.95 mM. The L-S system was structured with the liquid phase sandwiching the photocatalyst layer. The CO concentrations on both the upper and lower surfaces were set to 1.01 mM, representing the CO solubility saturation in aqueous solutions under standard conditions (25 °C, 1 atm).<sup>23</sup> In the G-L-S system, a sequence was established from top to bottom: the gas diffusion layer, photocatalyst layer, and the liquid phase. CO concentrations of 1.01 mM in aqueous solutions were applied to both upper and lower surfaces. For all models, the diffusion constant of water vapor in the gas phase was set as  $1.3 \times 10^{-5}$  m<sup>2</sup> s<sup>-1</sup>,<sup>24</sup>





while the diffusion constants of CO were set as follows:  $2.2 \times 10^{-5} \text{ m}^2 \text{ s}^{-1}$  in the gas phase,  $2.03 \times 10^{-9} \text{ m}^2 \text{ s}^{-1}$  in the aqueous phase, and  $2.4 \times 10^{-6} \text{ m}^2 \text{ s}^{-1}$  in the gas diffusion layer.<sup>34–36</sup>

## Conflicts of interest

The authors declare no conflict of interest.

## Acknowledgements

The authors are grateful for financial support from the National Key R&D Program of China (2021YFA1500803), the National Natural Science Foundation of China (51825205, 52120105002, 22272190, 22209190, 22088102), the Beijing Natural Science Foundation (2222035), the CAS Project for Young Scientists in Basic Research (YSBR-004), the DNL Cooperation Fund, CAS (DNL202016), the China Postdoctoral Science Foundation (2021M703288, 2021T150665), the Young Elite Scientist Sponsorship Program by CAST (2021QNRC001), and the Youth Innovation Promotion Association of the CAS.

## References

- 1 M. G. Rasul, M. A. Hazrat, M. A. Sattar, M. I. Jahirul and M. J. Shearer, The future of hydrogen: Challenges on production, storage and applications, *Energy Convers. Manage.*, 2022, **272**, 116326.
- 2 W. H. Chen and C. Y. Chen, Water gas shift reaction for hydrogen production and carbon dioxide capture: A review, *Appl. Energy*, 2020, **258**, 114078.
- 3 K. Ayers, N. Danilovic, R. Ouimet, M. Carmo, B. Pivovar and M. Bornstein, Perspectives on low-temperature electrolysis and potential for renewable hydrogen at scale, *Annu. Rev. Chem. Biomol. Eng.*, 2019, **10**, 219–239.
- 4 R. M. Navarro, M. A. Peña and J. L. G. Fierro, Hydrogen production reactions from carbon feedstocks fossil fuels and biomass, *Chem. Rev.*, 2007, **107**, 3952–3991.
- 5 J. D. Holladay, J. Hu, D. L. King and Y. Wang, An overview of hydrogen production technologies, *Catal. Today*, 2009, **139**, 244–260.
- 6 C. Ratnasamy and J. P. Wagner, Water gas shift catalysis, *Catal. Rev.: Sci. Eng.*, 2009, **51**, 325–440.
- 7 A. Ambrosi and S. E. Denmark, Harnessing the power of the water-gas shift reaction for organic synthesis, *Angew. Chem., Int. Ed.*, 2016, **55**, 12164–12189.
- 8 Y. X. Tong, L. Z. Song, S. B. Ning, S. X. Ouyang and J. H. Ye, Photocarriers-enhanced photothermocatalysis of water-gas shift reaction under H<sub>2</sub>-rich and low-temperature condition over CeO<sub>2</sub>/Cu<sub>1.5</sub>Mn<sub>1.5</sub>O<sub>4</sub> catalyst, *Appl. Catal., B*, 2021, **298**, 120551.
- 9 S. Y. Yao, X. Zhang, W. Zhou, R. Gao, W. Q. Xu, Y. F. Ye, L. L. Lin, X. D. Wen, P. Liu, B. B. Chen, E. Crumlin, J. G. Guo, Z. J. Zuo, W. Z. Li, J. L. Xie, I. Lu, C. Kiely, L. Gu, G. Shi, J. Rodriguez and D. Ma, Atomic-layered Au clusters on  $\alpha$ -MoC as catalysts for the low-temperature water-gas shift reaction, *Science*, 2017, **357**, 389–393.
- 10 Z. H. Zhang, X. Y. Chen, J. C. Kang, Z. Y. Yu, J. Tian, Z. M. Gong, A. P. Jia, R. You, K. Qian, S. He, B. T. Teng, Y. Cui, Y. Wang, W. H. Zhang and W. X. Huang, The active sites of Cu-ZnO catalysts for water gas shift and CO hydrogenation reactions, *Nat. Commun.*, 2021, **12**, 4331.
- 11 K. Xu, C. Ma, H. Yan, H. Gu, W. W. Wang, S. Q. Li, Q. L. Meng, W. P. Shao, G. H. Ding, F. R. Wang and C. J. Jia, Catalytically efficient Ni-NiO<sub>x</sub>-Y<sub>2</sub>O<sub>3</sub> interface for medium temperature water-gas shift reaction, *Nat. Commun.*, 2022, **13**, 2443.
- 12 Z. H. Cui, S. Song, H. B. Liu, Y. T. Zhang, F. Gao, T. Ding, Y. Tian, X. B. Fan and X. G. Li, Synergistic effect of Cu<sup>+</sup> single atoms and Cu nanoparticles supported on alumina boosting water-gas shift reaction, *Appl. Catal., B*, 2022, **313**, 121468.
- 13 Z. H. Zhang, S. S. Wang, R. Song, T. Cao, L. F. Luo, X. Y. Chen, Y. X. Gao, J. Q. Lu, W. X. Li and W. X. Huang, The most active Cu facet for low-temperature water gas shift reaction, *Nat. Commun.*, 2017, **8**, 488.
- 14 Y. J. Zhang, C. Q. Chen, X. Y. Lin, D. L. Li, X. H. Chen, Y. Y. Zhan and Q. Zheng, CuO/ZrO<sub>2</sub> catalysts for water-gas shift reaction: Nature of catalytically active copper species, *Int. J. Hydrogen Energy*, 2014, **39**, 3746–3754.
- 15 J. L. Santos, T. R. Reina, S. Ivanova, M. A. Centeno and J. A. Odriozola, Gold promoted Cu/ZnO/Al<sub>2</sub>O<sub>3</sub> catalysts prepared from hydrotalcite precursors: Advanced materials for the WGS reaction, *Appl. Catal., B*, 2017, **201**, 310–317.
- 16 L. Torrente-Murciano and F. R. Garcia-Garcia, Effect of nanostructured support on the WGS activity of Pt/CeO<sub>2</sub> catalysts, *Catal. Commun.*, 2015, **71**, 1–6.
- 17 A. Kubacka, M. Fernandez-García and G. Colón, Advanced nanoarchitectures for solar photocatalytic applications, *Chem. Rev.*, 2012, **112**, 1555–1614.
- 18 Y. Ma, X. L. Wang, Y. S. Jia, X. B. Chen, H. X. Han and C. Li, Titanium dioxide-based nanomaterials for photocatalytic fuel generations, *Chem. Rev.*, 2014, **114**, 9987–10043.
- 19 L. K. Zhao, Y. H. Qi, L. Z. Song, S. B. Ning, S. X. Ouyang, H. Xu and J. H. Ye, Solar-driven water-gas shift reaction over CuO<sub>x</sub>/Al<sub>2</sub>O<sub>3</sub> with 1.1% of light-to-energy storage, *Angew. Chem., Int. Ed.*, 2019, **58**, 7708–7712.
- 20 F. Sastre, M. Oteri, A. Corma and H. García, Photocatalytic water gas shift using visible or simulated solar light for the efficient, room-temperature hydrogen generation, *Energy Environ. Sci.*, 2013, **6**, 2211–2215.
- 21 N. Liu, M. Xu, Y. S. Yang, S. M. Zhang, J. Zhang, W. L. Wang, L. R. Zheng, S. Hong and M. Wei, Au<sup>δ</sup>-Ov-Ti<sup>3+</sup> interfacial site: catalytic active center toward low-temperature water gas shift reaction, *ACS Catal.*, 2019, **9**, 2707–2717.
- 22 X. C. Ma, Y. L. Shi, J. Y. Liu, X. T. Li, X. F. Cui, S. J. Tan, J. Zhao and B. Wang, Hydrogen-bond network promotes water splitting on the TiO<sub>2</sub> surface, *J. Am. Chem. Soc.*, 2022, **144**, 13565–13573.
- 23 K. S. Davidge, R. Motterlini, B. E. Mann, J. L. Wilson and R. K. Poole, Carbon monoxide in biology and microbiology: Surprising roles for the “detroit perfume”, *Adv. Microb. Physiol.*, 2009, **56**, 85–167.





- 24 E. L. Cussler, *Diffusion: Mass Transfer in Fluid Systems*, Cambridge university press, Cambridge, 3rd edn, 2009.
- 25 H. N. Huang, R. Shi, Z. H. Li, J. Q. Zhao, C. L. Su and T. R. Zhang, Triphase photocatalytic CO<sub>2</sub> reduction over silver-decorated titanium oxide at a gas-water boundary, *Angew. Chem., Int. Ed.*, 2022, e202200802.
- 26 X. Y. Xiong, Z. P. Wang, Y. Zhang, Z. H. Li, R. Shi and T. R. Zhang, Wettability controlled photocatalytic reactive oxygen generation and *Klebsiella pneumoniae* inactivation over triphase systems, *Appl. Catal., B*, 2020, **264**, 118518.
- 27 L. J. Li, L. P. Xu, Z. F. Hu and J. C. Yu, Enhanced mass transfer of oxygen through a gas-liquid-solid interface for photocatalytic hydrogen peroxide production, *Adv. Funct. Mater.*, 2021, **31**, 2106120.
- 28 H. Song, X. G. Meng, Z. J. Wang, Z. Wang, H. L. Chen, Y. X. Weng, F. Ichihara, M. Oshikiri, T. Kako and J. H. Ye, Visible-light-mediated methane activation for steam methane reforming under mild conditions: A case study of Rh/TiO<sub>2</sub> catalysts, *ACS Catal.*, 2018, **8**, 7556–7565.
- 29 Y. J. Chen, S. F. Ji, W. M. Sun, Y. P. Lei, Q. C. Wang, A. Li, W. X. Chen, G. Zhou, Z. D. Zhang, Y. Wang, L. R. Zheng, Q. H. Zhang, L. Gu, X. D. Han, D. S. Wang and Y. D. Li, Engineering the atomic interface with single platinum atoms for enhanced photocatalytic hydrogen production, *Angew. Chem., Int. Ed.*, 2020, **59**, 1295–1301.
- 30 Y. L. Chen, X. Q. Liu, L. Hou, X. R. Guo, R. W. Fu and J. M. Sun, Construction of covalent bonding oxygen-doped carbon nitride/graphitic carbon nitride Z-scheme heterojunction for enhanced visible-light-driven H<sub>2</sub> evolution, *Chem. Eng. J.*, 2020, **383**, 123132.
- 31 C. C. Han, P. F. Su, B. H. Tan, X. G. Ma, H. Lv, C. Y. Huang, P. Wang, Z. F. Tong, G. Li, Y. Z. Huang and Z. F. Liu, Defective ultra-thin two-dimensional g-C<sub>3</sub>N<sub>4</sub> photocatalyst for enhanced photocatalytic H<sub>2</sub> evolution activity, *J. Colloid Interface Sci.*, 2021, **581**, 159–166.
- 32 H. F. Wei, H. Liu, L. Yu, M. Zhang, Y. L. Zhang, J. C. Fan, X. J. Cui and D. H. Deng, Alloying Pd with Cu boosts hydrogen production via room-temperature electrochemical water-gas shift reaction, *Nano Energy*, 2022, **102**, 107704.
- 33 X. Zhang, M. T. Zhang, Y. C. Deng, M. Q. Xu, L. Artiglia, W. Wen, R. Gao, B. B. Chen, S. Y. Yao, X. C. Zhang, M. Peng, J. Yan, A. W. Li, Z. Jiang, X. Y. Gao, S. F. Cao, C. Yang, A. J. Kropf, J. N. Shi, J. L. Xie, M. S. Bi, J. A. van Bokhoven, Y. W. Li, X. D. Wen, M. Flytzani-Stephanopoulos, C. Shi, W. Zhou and D. Ma, A stable low-temperature H<sub>2</sub>-production catalyst by crowding Pt on alpha-MoC, *Nature*, 2021, **589**, 396–401.
- 34 P. Wang, J. Q. Zhao, R. Shi, X. R. Zhang, X. D. Guo, Q. Dai and T. R. Zhang, Efficient photocatalytic aerobic oxidation of bisphenol A via gas-liquid-solid triphase interfaces, *Mater. Today Energy*, 2022, **23**, 100908.
- 35 I. Amdur and L. M. Shuler, Diffusion coefficients of the systems CO-CO and CO-N<sub>2</sub>, *J. Chem. Phys.*, 1963, **38**, 188–192.
- 36 D. H. Shou, J. T. Fan, M. F. Mei and F. Ding, An analytical model for gas diffusion through nanoscale and microscale fibrous media, *Microfluid. Nanofluid.*, 2014, **16**, 381–389.

